# Transcranial Focusing of Ultrasonic Vortices by Acoustic Holograms

Sergio Jiménez-Gambín, Noé Jiménez,[*] and Francisco Camarena
*Instituto de Instrumentación para Imagen Molecular, Universitat Politècnica de València, CSIC,*
*Camino de Vera S/N, València 446085, Spain*

Acoustic vortex beams have great potential for contactless particle manipulation and torque-based biomedical applications. However, focusing acoustic waves through highly aberrating layers such as the human skull at ultrasonic frequencies results in strong phase aberrations, which prevent the generation of sharp acoustic images. In the case of a wavefront containing phase dislocations, skull aberrations can inhibit the focusing of acoustic vortex beams inside the cranial cavity. In this paper, we demonstrate that phase-conjugated acoustic holograms can encode time-reversed fields, allowing compensation of the aberrations of the skull and, simultaneously, the generation of a focused vortex inside an *ex vivo* human skull. The method is applied to single-element geometrically focused sources and results in a very simple and compact ultrasonic system. This work will pave the way to designing low-cost particle-trapping systems, clot manipulation, and the exertion of acoustic-radiation forces and torques in the brain for biomedical applications.

## I. INTRODUCTION

Focused ultrasound is emerging as a robust approach to the treatment of a broad range of neurological diseases. Finite-amplitude focused ultrasound beams can induce localized temperature rises and are currently used for thermal ablation of deep-brain nuclei [1]. In addition, ultrasound beams carry linear momentum that can be transferred to tissues, intracorporeal fluids, and small objects, enabling a broad range of techniques based on noninvasive mechanical effects. These include therapeutic applications such as localized neuromodulation [2], targeted drug delivery in the brain [3], and imaging techniques such as transcranial elastography [4].

In addition to the linear momentum carried by conventional ultrasound beams, acoustic vortex beams carry angular orbital momentum [5,6]. Acoustic vortex beams are collimated wavefronts exhibiting phase dislocations, whose phase is proportional to $e^{il\phi}$, where $\phi$ is the azimuthal angle and $l$ is the topological charge. The field exhibits a phase singularity on the beam axis and therefore vanishes at this point due to destructive interference. Acoustic vortex beams can transfer their angular momentum to microscopic and macroscopic solid objects [7–12] and to fluids [13] and exert mechanical torques on them. In addition, the singular scattering of vortex beams by small particles produces trapping acoustic-radiation forces, resulting in practical applications in contactless particle

tweezing and manipulation [14–17]. It is worth noting here that acoustic vortices can exert mechanical forces several orders of magnitude higher than those exerted by their optical counterparts, with lower induced thermal effects [18,19], and, furthermore, acoustic vortices can propagate deeply through opaque media such as biological tissues. Acoustic vortices have recently shown their potential to manipulate individual cells without inducing photothermal and/or photochemical damage [20], to trap and guide kidney-stone fragments [21], and to selectively guide individual drug-delivery carriers based on microbubbles [22].

As phase dislocations are the basis of these techniques, the wavefront must be controlled with accuracy. Several methods to synthesize vortex beams have been reported, including active sources or phased arrays [6,23–25], transducers with helical geometries [23,26], Archimedean-spiral [27,28] or Fresnel-spiral diffraction gratings [29], systems exploiting the photoacoustic effect [30], active vibrating surfaces with spiral shapes [31], and metamaterials exhibiting local resonances [32–36]. Of special interest for wavefront engineering are acoustic holograms [37]. Acoustic holograms can be used to generate vortex beams with great accuracy by encoding information about the full wavefront into the manufactured lens [38].

However, when they are focused into the brain, ultrasound beams experience strong refraction and attenuation due to the complex structure and irregular shape of the skull bones. In this way, the skull introduces strong aberrations that distort the wavefront, decreasing the focusing performance of conventional single-element approaches. One strategy to solve this problem is to directly bypass the

---

[*]nojigon@upv.es

skull bones by using small invasive ultrasound implants located within the skull after partial craniotomy [39,40]. This approach can be applied to enhance the delivery of chemotherapeutic agents after open surgery; however, in other circumstances, the need for craniotomy leads to serious complications and drawbacks. Noninvasive approaches include phased-array systems guided with magnetic resonance imaging, which allow the focusing of ultrasound with great accuracy and allow beam steering, and the aberrations of the skull can be mitigated by tuning the phase of each individual emitter [3,41]. However, as the separation between individual elements in these systems is typically much larger than half a wavelength, these systems show strong grating lobes when the beam is steered far from its geometrical focus, and, in addition, these systems are complex and expensive.

To tackle this problem, structures showing local resonances, i.e., metamaterials, have been theoretically proposed in two dimensions to compensate the aberrations of a layer mimicking the skull [42], but their application in a realistic situation has not been demonstrated yet. Recently, 3D-printed acoustic lenses have been proposed to compensate the aberrations of the skull by focusing ultrasound beams at one single focal spot [43]. The full potential of 3D-printed lenses for complex wavefront engineering can be unleashed by using acoustic holograms [44]. By synthesizing complex wavefronts, acoustic holograms can efficiently compensate skull aberrations and, simultaneously, form arbitrary acoustic images adapted to the desired therapeutic target. In addition, as the pixel density is much larger than that in state-of-the-art phased arrays for therapeutic ultrasound, acoustic holograms also

allow wide-angle beam steering without grating lobes [44].

In this paper, we demonstrate that acoustic vortices can be focused through an *ex vivo* human skull by using acoustic holograms. Using personalized 3D-printed holograms, the phase aberrations produced by the skull can be compensated, and an acoustic beam containing phase dislocations can be focused into the cranial cavity.

## II. HOLOGRAM GENERATION

The system is composed of a spherically focused piezoelectric transducer, custom made with a focal length $F_0 = 140$ mm and an aperture $2a_0 = 100$ mm, with a nominal frequency $f_0 = 500$ kHz, as sketched in Fig. 1(a). We design two holographic lenses, one for a homogeneous medium (water) and one for a medium including the human skull. A detailed description of the setup is given in Appendix C.

For the vortex hologram designed for a homogeneous medium, in the source plane $z = 0$, where the polar coordinates are given by $\mathbf{r}_0 = \mathbf{r}(r, \phi)$, a geometrical approximation to the phase profile of a diverging wavefront with a rotational phase is given by $H_0 = \exp(-ik\sqrt{r^2 + F^2})\exp(il\phi)$, where $k = 2\pi f_0/c_0$ is the wave number in a homogeneous medium with sound speed $c_0$, $l$ is the topological charge of the vortex, and $F$ is the desired focal distance. The spherically focused transducer already introduces a fixed focusing phase profile, which is given by $H_s = \exp(ik_L\sqrt{r^2 + F_0^2})$, where $k_L = 2\pi f_0/c_L$ and $c_L$ is the sound speed in the material of the lens. Finally, the phase-conjugated hologram in the holographic
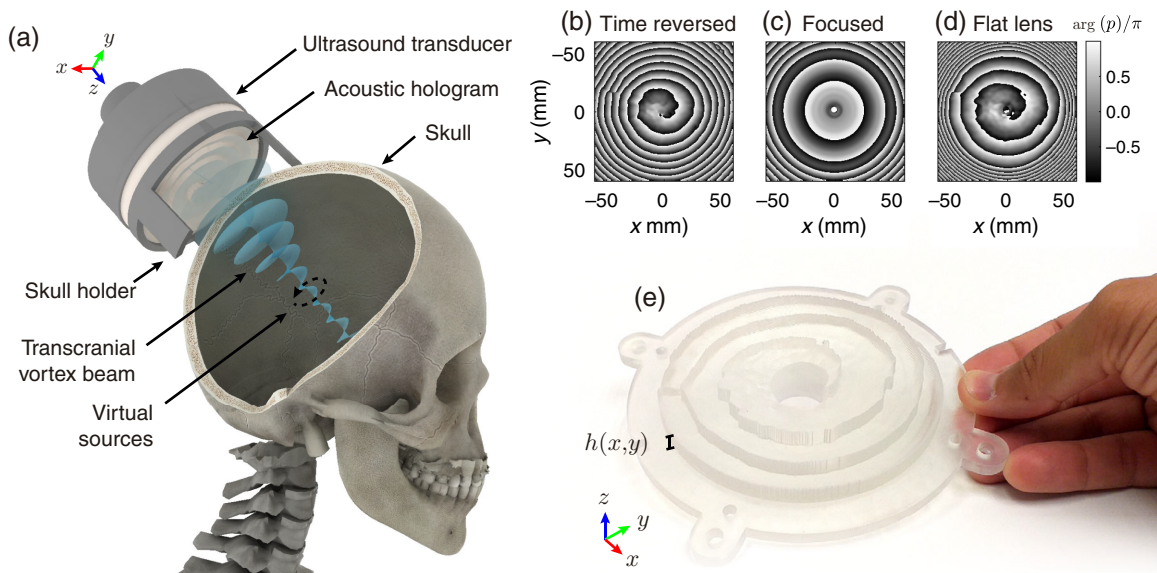


FIG. 1. (a) Scheme of the setup. (b) Backward-simulated field in the holographic plane, $H_0(x, y)$. (c) Field of the focused source, $H_s(x, y)$. (d) Phase-conjugated holographic field, $H(x, y)$. (e) 3D-printed acoustic hologram for the geometrically focused transducer.

plane is given by $H = H_0^* H_s^*$, where $(\cdot)^*$ denotes complex conjugation.

To design the hologram to include the aberrating layer of the skull, we make use of a time-reversal method. The process essentially follows the procedure described in Ref. [44]. We start by scanning an *ex vivo* human skull using x-ray computed tomography (CT) with a resolution of $0.33 \times 0.33 \times 1.25$ mm³, after the scalp is removed whole with a scalpel. Volumetric Hounsfield data are converted to bone-density and sound-speed values using empirical relations [45,46]. Then, this tomographic information is used in a time-reversal simulation based on pseudospectral time-domain methods [47], including a *k*-space corrector and a spectral approximation to the fractional Laplacian to model the frequency-power-law attenuation observed in biological tissues [48,49]. For the backward-simulation step in the time-reversal approach, a set of 30 virtual sources are located on a ring of radius $r_s = 2.5$ mm $(0.83\lambda)$ in the plane $z_s = F = 97.4$ mm $(33\lambda)$, centered at $x = y = 0$, as sketched in Fig. 1(a). Each source is set to emit a sinusoidal signal with a complex amplitude proportional to $\exp(il\theta)$. Then, the acoustic field $H_0(x, y)$ is recorded in the holographic plane located in the exit plane of the transducer, given by $z_0 = F_0 - \sqrt{F_0^2 - a_0^2}$, resulting in the phase distribution shown in Fig. 1(b). To compensate for the geometrical focusing of the bowl-shaped source (note that $F \neq F_0$), we perform an additional simulation for the focused source in the absence of the skull, and we measure the field $H_s(x, y)$ in the exit plane $z_0$. The retrieved phase distribution, $H_s$, is shown in Fig. 1(c), showing the characteristic Fresnel rings. The final hologram is designed as previously, using $H = H_0^* H_s^*$. The phase distribution is shown in Fig. 1(d), where the spiraling pattern due to the

focused vortex and the wavy distortions produced by the aberrations of the skull can be visually identified.

To design the two lenses, we model each pixel of the surface of the hologram as an elastic Fabry-Perot resonator of height $h(x, y)$, as shown in Fig. 1(e). Their complex frequency-dependent transmission coefficient, measured in the output source plane $z_0$, is given by [44]

$$T(x, y) = \frac{2Z_n \exp[-ik(z_0 - h)]}{2Z_n \cos(k_L h) + i(Z_n^2 + 1)\sin(k_L h)}, \quad (1)$$

where $Z_n = Z_0/Z_L$ is the normalized impedance, $Z_0 = \rho_0 c_0$ and $\rho_0$ are the impedance and density, respectively, of the water, and $Z_L = \rho_L c_L$ and $\rho_L$ are the impedance and density, respectively, of the lens. By changing the height of each pixel $h(x, y)$, the phase of the transmitted waves $T(x, y)$ can be varied from 0 to $2\pi$. To fit the phase of the transmitted waves to the phase of the target hologram, we look for an $h(x, y)$ that fulfills $\arg(T) = \arg(H)$, making use of an interpolation method because Eq. (1) cannot be inverted [44]. As a result, we obtain the height of each of the pixels that are used to construct the hologram for the focused source. The final 3D-printed lens for the transcranial configuration is shown in Fig. 1(e). After the lens is designed and manufactured, its performance is analyzed by estimating the acoustic field using a forward simulation and experimental measurements in a water tank (see Appendix C for further details).

## III. RESULTS

### A. Vortices in a homogeneous medium

The acoustic field generated by the lens for a homogeneous medium is shown in Fig. 2. The magnitude of the
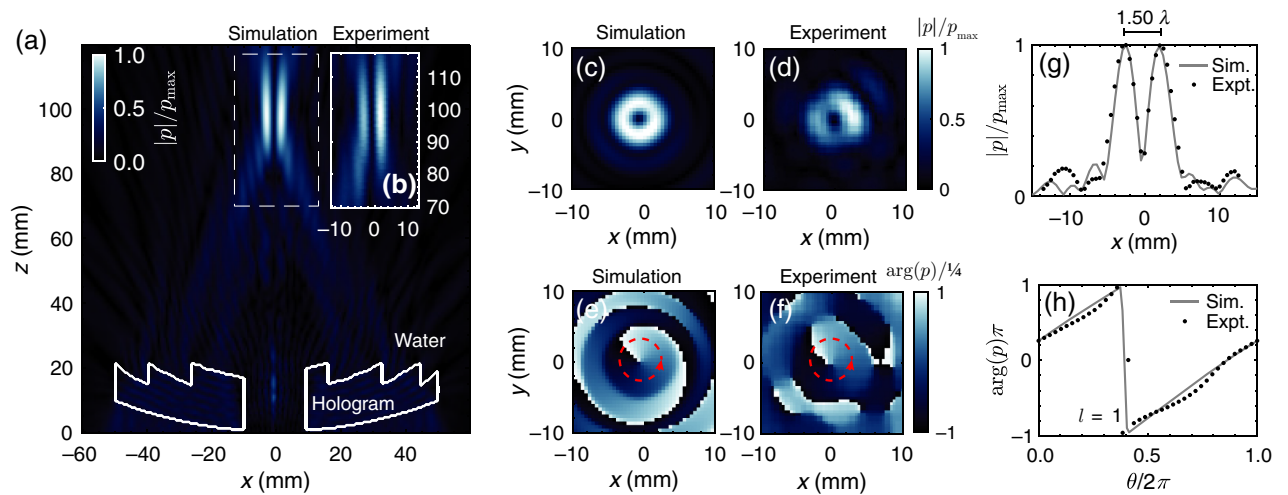


FIG. 2. Field of the vortex hologram $(l = 1)$ designed for a homogeneous medium. (a) Simulated and (b) experimental normalized sagittal cross section of the field at $y = 0$. (c),(d) Magnitude and (e),(f) phase of a transverse cross section of the field obtained at $z = F$. (g) Normalized magnitude of the field at $z = F$ and $y = 0$. (h) Normalized phase of the field versus the azimuthal angle.

acoustic-pressure sagittal field ($|p(x, 0, z)|/p_{max}$) is shown in Fig. 2(a) for the simulation and the experiment. We can identify that the designed hologram generates a void-containing beam whose pressure peaks around the focal distance ($z = 96.9$ mm for the simulation and $z = 97.0$ mm for the experiment). Note the geometrical focal distance of the source is $F_0 = 140$ mm. The transverse field profiles measured at $z = F$ are given in Figs. 2(c)–2(f). The magnitudes of the simulated and experimental fields [Figs. 2(c) and 2(d)] show a ring-shaped distribution, and at its center the field vanishes. The null is caused by the phase singularity at the focal spot, which is clearly visible in Figs. 2(e) and 2(f) for the simulation and the experiment, respectively. In addition, we can identify that the phase singularity is the result of a screw dislocation produced by the counterclockwise rotation of the phase, marked by the red arrows. In Fig. 2(g), the magnitude of the field is shown in detail for a transverse section. The experimental and simulated fields agree, and the beam shows a width of 1.5 times the wavelength at the nominal frequency. Finally, the phase as a function of the azimuthal angle at a radial distance of 2.21 mm, corresponding to the beam width, is shown in Fig. 2(h). The generated transverse field shows a levorotatory phase distribution whose phase rotates as a function of the azimuthal angle at a rate given by the topological charge, $l = 1$. Therefore, the phase rotates by $2\pi$ radians in a complete azimuthal turn, showing that the proposed lenses for moderately focused sources can form acoustic vortices with great accuracy.

### B. Vortex synthesis for transcranial propagation

We proceed to present the results for the lens designed for transcranial propagation, summarized in Fig. 3.

Figure 3(a) shows the experimental setup, where the skull is immersed in a water tank and the acoustic field is scanned in several planes using a hydrophone. A skull holder is 3D printed to ensure correct positioning of the lens with respect to the surface of the skull. The irregular shape of the skull ensures that the holder can be correctly located only at the design position. The retrieved acoustic field is shown in Figs. 3(b) and 3(c) for the simulation and the experiment, respectively. The phase-only hologram is able to encode the time-reversed field with great accuracy. It compensates the aberrations of the skull while, simultaneously, it modifies the wavefront to generate a focused vortex by introducing a quasiparabolic phase profile with a rotational profile. In addition, the simulation and experimental results are in good agreement. The pressure peaks at $z = 96.9$ mm in the simulation and $z = 97.5$ mm in the experiment. The transverse cross sections of the field at $z = F$ are shown in Figs. 2(d)–2(g). The transverse field magnitude [Figs. 2(d) and 2(e)] shows a ring-shaped distribution similar to that obtained for a homogeneous medium. The magnitude of the field vanishes at the center in both the experimental and the simulated results. The corresponding phase distribution is shown in Figs. 3(f) and 3(g). A counterclockwise rotation is achieved in the focal plane, and a phase singularity is visible at the location of the null.

Note that in the absence of the skull, the simulated peak pressure is $7.7p_0$, where $p_0$ is the pressure at the surface of the transducer. When the skull is introduced, the simulated peak pressure decreases to $4.0p_0$. In this way, the amplitude of the vortex decreases by a factor of 1.9 (5.6 dB) when the skull is introduced.

A detailed picture is shown in Fig. 4. The magnitude of the transverse cross section of the field is shown in Fig. 4(a). The experimental data agree with the simulation
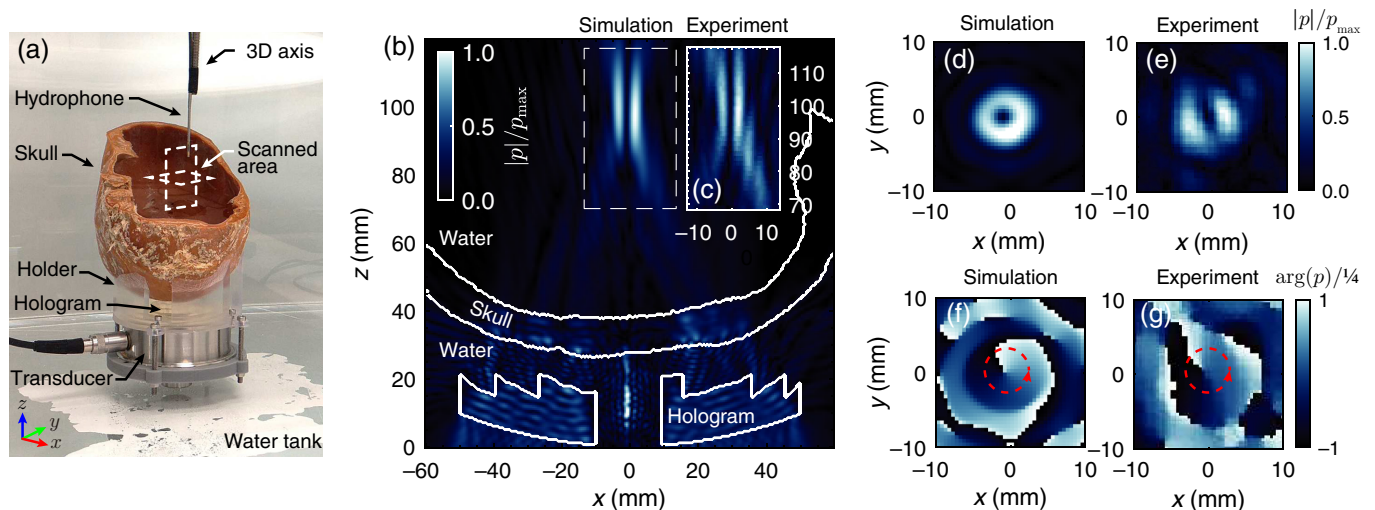


FIG. 3. Field of the vortex hologram ($l = 1$) designed for a transcranial-propagation medium. (a) Scheme of the experimental setup. (b) Simulated and (c) experimental normalized sagittal cross section of the field at $y = 0$. (d),(e) Magnitude and (f),(g) phase of a transverse cross section of the field obtained at $z = F$.
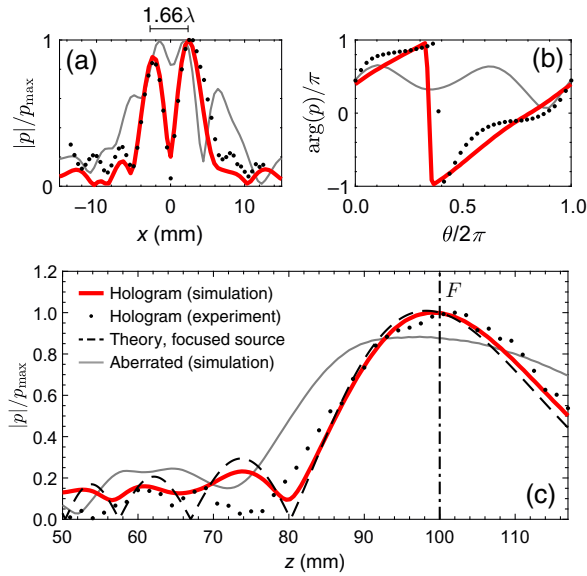
FIG. 4. (a) Normalized magnitude of the field at $z = F$ and $y = 0$. (b) Normalized phase of the field versus the azimuthal angle. (c) Axial cross section of the field measured at $y = 0$ and $x = 2.21$ mm.

results for this cross section. The experimental transverse width of the beam is 5 mm ($1.66\lambda$), of the order of the value reached for the lens designed for a homogeneous medium. The experiment shows some discrepancies with the simulation [already visible when Figs. 3(d) and 3(e) are compared]. However, it is worth noting here that when the hologram designed for a homogeneous medium is used for the transcranial configuration [gray curve in Fig. 4(a)], the aberrations distort the wavefront and a null is not observed. The phase of the field as a function of the azimuthal angle is shown in Fig. 4(b). The phase of the field generated with the transcranial hologram, in both the experiment and the simulation, rotates by $2\pi$ radians in a whole azimuthal turn. In contrast, the phase retrieved for the lens designed for a homogeneous medium does not show a screw dislocation, because the aberrations of the skull distort the wavefront and prevent vortex generation. Finally, the longitudinal cross section of the field along the axial coordinate, measured at $y = 0$ and $x = 2.5$ mm (matching the peak pressure location), is shown in Fig. 4(c). The experimental and simulated data for the transcranial hologram are also roughly in agreement with the theoretical field of a focused source, given by $|p(\tilde{z})| = 2p_0 \left| \sin\left[ G(1 - \tilde{z})/(2\tilde{z}) \right] / (1 - \tilde{z}) \right|$, where $\tilde{z} = z/F$ and $G = ka^2/2F$. The focusing performance of the hologram is limited by the natural diffraction of waves, as occurs with any finite-aperture focused acoustic source. In contrast, the aberrations produced by the skull distort the wavefront, leading to a decrease in the focusing performance of the ultrasonic system.

## IV. CONCLUSIONS

The human skull introduces strong attenuation and refraction when ultrasonic waves propagate through it, resulting in aberrations that prevent the focusing of acoustic vortices at ultrasonic frequencies. Acoustic holograms, as presented in this paper, are able to physically encode time-reversed fields containing phase dislocations with great accuracy using very simple and compact ultrasonic systems. On the one hand, acoustic holograms allow one to compensate the aberrations of the skull, and, on the other hand, they simultaneously tune the phase of the wavefront to generate a focused vortex by introducing a quasiparabolic phase with a rotational phase profile. This results in a personalized single-element system that is able to focus a vortex inside the human skull.

As the size of the acoustic vortices is limited by the natural diffraction of acoustic waves, it can be adjusted by changing the aperture and frequency of the source, i.e., by tuning the angular spectrum of the field encoded by the hologram. In this situation, a personalized hologram must be obtained for each ultrasound source and patient to obtain better targeting accuracy. In addition, we present a method to design holograms for geometrically focused sources. Extending this design to vortices with higher topological charges is also feasible; see the results in Appendix D.

One might note that due to the isoplanatic angles of the aberrating skull, the correction of aberrations can be maintained to some degree even if the source is moved with respect to the patient's head, as demonstrated recently for focused beams [50]. Therefore, the holographic system described here might be used to manipulate small particles and objects *in vivo* by mechanically steering the hologram-source system to move the vortex location. In this situation, an additional technology would need to be used to detect and locate the target, e.g., a clot. Portable ultrasonic methods or other imaging technologies as CT or magnetic resonance imaging could be applied, and used to feed the mechanical steering system and to trigger the power amplifier.

In addition, angular momentum can be transferred to tissues by focusing acoustic vortices. Aberration-free holographic acoustic vortices open up ways to implement biomedical applications of ultrasound beyond the transfer of linear momentum, allowing the transfer of angular momentum to the brain. The biological response of central-nervous-system (CNS) tissues to the angular momentum produced by focused vortices remains unexplored. Other effects such as neuromodulation or blood-brain-barrier opening by trapping a cluster of bubbles inside the CNS using vortices might be studied in future work, thanks to acoustic holograms. In this way, the present work will pave the way to designing low-cost particle-trapping systems, clot manipulation, torque exertion in

the brain, and acoustic-radiation-force-based biomedical applications, opening up a path to exploring the biological response of tissues to therapeutic ultrasonic vortex beams.

## ACKNOWLEDGMENTS

## APPENDIX A: SIMULATION METHODS

We use a pseudospectral simulation method including a $k$-space dispersion corrector to numerically integrate the linearized constitutive relations of acoustics [48,49]. In an inhomogeneous and absorbing medium, the governing equations, i.e., the continuity equation, the momentum-conservation equation, and the pressure-density relation, can be written as three coupled first-order partial differential equations as follows:

$$\frac{\partial \rho}{\partial t} = -\rho_0 \nabla \cdot \mathbf{u} - \mathbf{u} \cdot \nabla \rho_0, \tag{A1}$$

$$\frac{\partial \mathbf{u}}{\partial t} = -\frac{1}{\rho_0} \nabla p, \tag{A2}$$

$$p = c_0^2 \left( \rho + \mathbf{d} \cdot \nabla \rho_0 - L\rho \right), \tag{A3}$$

where $\mathbf{u}$ is the acoustic particle velocity, $\mathbf{d}$ is the acoustic particle displacement, $p$ is the acoustic pressure, $\rho$ is the acoustic density, $\rho_0$ is the ambient (or equilibrium) density, $c_0$ is the sound speed, and $L(\mathbf{r}, t)$ is a linear operator introducing the frequency-dependent absorption and dispersion [48].

Tissue absorption, following a power law with respect to frequency given by $\alpha(\omega) = \alpha_0 \omega^\gamma$, where $\alpha_0$ is the absorption coefficient and $\gamma$ is the exponent of the frequency power law, together with its corresponding physical dispersion, is included by use of an integrodifferential operator as follows:

$$L = \tau \frac{\partial}{\partial t} \left( -\nabla^2 \right)^{(\gamma/2)-1} + \eta \left( -\nabla^2 \right)^{[(\gamma+1)/2]-1}, \tag{A4}$$

where $\tau = -2\alpha_0 c_0^{\gamma-1}$ and $\eta = 2\alpha_0 c_0^\gamma \tan(\pi\gamma/2)$ are the absorption and dispersion proportionality coefficients,

respectively. This operator is solved efficiently using a fractional Laplacian in $k$ space. This simulation method is selected because it provides low numerical dispersion as compared with finite-difference methods [51]. We use a numerical grid with a spatial step of $\Delta x = \Delta y = \Delta z = 0.5$ mm and a numerical temporal step of $\Delta t = 33.2$ ns, leading to a Courant-Friedrichs-Lewy number of 0.10 in water and a spatial sampling of six grid points per wavelength in water at 0.5 MHz. These parameters are fixed in all simulations presented in this paper.

The original resolution of the CT scan for the acquisition of data on the human skull, of $0.33 \times 0.33 \times 1.25$ mm$^3$, is interpolated using a cubic interpolation method to an isotropic grid of size 0.5 mm ($\lambda/6$) for the simulations.

## APPENDIX B: LENS DESIGN

The design of the holographic acoustic lenses is based on a time-reversal method. First, a backward simulation is performed by setting the target acoustic image as the virtual source, and the resulting field is recorded at the holographic surface. The phase-conjugated recorded pressure distribution at the working frequency is used to design the physical lens. Any effects due to the heterogeneous medium between the target and the transducer are taken into account, and both the direct field and multiple reflections are encoded by the hologram. Then, the wave-field information is encoded in each pixel of the lens by assuming that each pixel vibrates longitudinally as an elastic Fabry-Perot resonator. By setting the height of each pixel, the phase of the transmission coefficient is matched to the phase of the recorded field following the procedure described in Ref. [44]. The lens surface is divided into square pixels of area $0.5 \times 0.5$ mm$^2$. Therefore, the designed holographic acoustic lenses, with a central hole, have a total of 31 084 elements each, thus allowing accurate control of the holographic wavefront.

The holographic acoustic lenses are numerically designed and afterwards manufactured using a 3D-printing stereolithographic technique (stereolithography), employing a Form 2 printer (Formlabs, USA) with a resolution of 50 and 100 $\mu$m in the lateral and axial directions, respectively, and using a photosensitive resin (Standard Clear, Formlabs, USA). The acoustical properties of the material are obtained experimentally using a pulse-echo technique in a test cylinder, resulting in a measured sound speed $c_L = 2580$ m/s, a density $\rho_L = 1171$ kg/m$^3$, and an absorption $\alpha = 1.38$ dB/cm at 0.5 MHz, matching the reported values for similar polymers [37,52].

## APPENDIX C: EXPERIMENTAL METHODS

The experimental setup is sketched in Fig. 5. The experiments are conducted in a $0.80 \times 0.43 \times 0.63$ m$^3$ water tank filled with degassed and distilled water at 26 °C. The ultrasound emitter is composed of a spherically focused
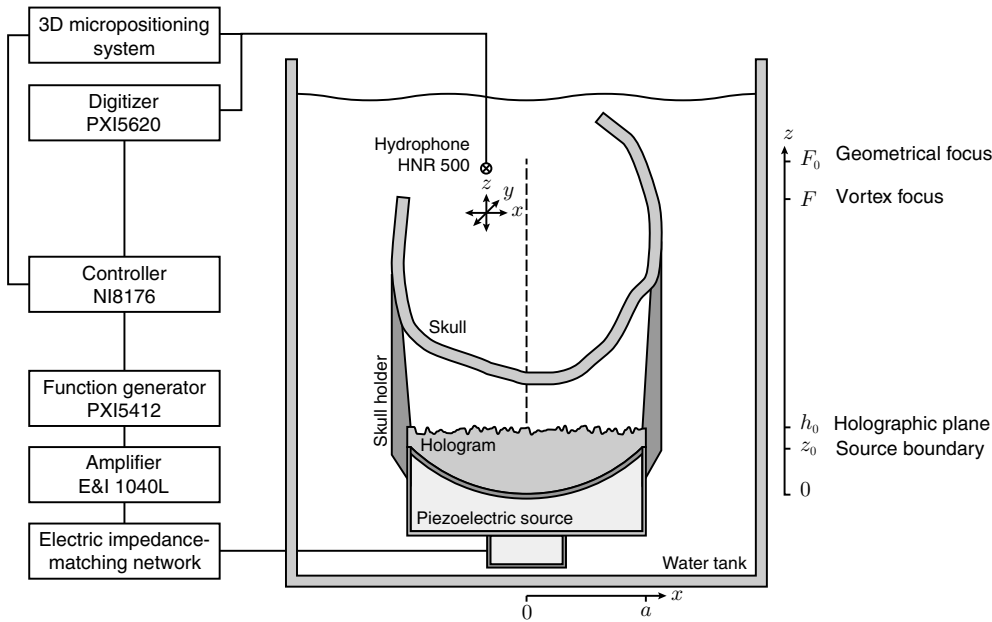
FIG. 5. Scheme of the experimental setup.

piezoelectric transducer, custom made with a focal length $F_0 = 140$ mm and an aperture $2a_0 = 100$ mm, with a nominal frequency $f_0 = 500$ kHz, mounted in a custom-designed stainless-steel housing. A custom-made electric-impedance-matching network is used to maximize the power delivered to the transducer. The transducer is driven with a 20-cycle sinusoidal pulse burst at a frequency $f = 0.5$ MHz by a function generator (14 bits, 100 MS/s (million samples per second), model PXI5412, National Instruments) and amplified by a linear rf amplifier (ENI 1040L, 400 W, 55 dB, ENI, Rochester, NY, USA). The pressure field is measured by a needle hydrophone with a 500-$\mu$m active diameter (model HNR-500, Onda, Sunnyvale, CA, USA). The source amplitude is set low enough to avoid any nonlinear effects during propagation. The hydrophone signals are digitized at a sampling rate of 64 MHz by a digitizer (model PXI5620, National Instruments) and averaged 20 times to increase the signal-to-noise ratio. A three-dimensional micropositioning system (controller model C-884 and three L-511 orthogonal linear stages, PI miCos GmbH, Germany) is used to move the hydrophone in three orthogonal directions with an accuracy of 10 $\mu$m. The scanning area for the sagittal cross sections, $p(x, z)$, covers a range from $-12$ to $12$ mm in the $x$ direction and from 69 to 115 mm in the $z$ direction, using step sizes of 0.5 and 1 mm, respectively, and the scanning area for the transverse cross-section planes, $p(x, y)$, covers a range from $-12$ to $12$ mm in both the $x$ and the $y$ directions, using a step size of 0.5 mm. All the signal-generation and acquisition processes are based on an NI8176 National Instruments PXI-Technology controller, which also controls the micropositioning system. Temperature measurements are performed throughout the whole process to ensure no temperature changes of more than 0.5 °C.

The sound speed in the water is $c_0 = 1475$ m/s (at a temperature of 17.7 °C in the tank), the density is $\rho_0 = 1000$ kg/m³, and the absorption is $\alpha_0 = 0.59 \times 10^{-3}$ dB/cm at 0.5 MHz. For the *ex vivo* human skull, the sound speed ranges from $c_0$ to $c_{\max} = 2958$ m/s, with an average of $c_{\mathrm{mean}} = 2149$ m/s, and the density ranges from $\rho_0$ to $\rho_{\max} = 2086$ kg/m³, with an average of $\rho_{\mathrm{mean}} = 1494$ kg/m³, matching the values reported in the literature [53,54]. The absorption of the skull is set to a value $\alpha_{\mathrm{skull}} = 5.21$ dB/cm at 0.5 MHz [55].

## APPENDIX D: TRANSCRANIAL VORTICES WITH HIGH-ORDER TOPOLOGICAL CHARGE

More complex vortex holograms are numerically designed to demonstrate the feasibility of using this method to generate higher-topological-charge acoustic vortices. In particular, a topological charge of $l = 2$ is chosen. For the backward-simulation step in the time-reversal approach, a set of 44 virtual sources are located on a ring of radius $r_s = 4.1$ mm ($1.39\lambda$) in the plane $z_s = F = 97.4$ mm ($33\lambda$), centered at $x = y = 0$. Each source is set to emit a sinusoidal signal with a complex amplitude proportional to $\exp(il\theta)$, with $l = 2$.

A comparison of the simulated acoustic fields generated by the lenses for both homogeneous and aberrating media is shown in Fig. 6. The magnitudes of the acoustic-pressure sagittal fields ($|p(x, 0, z)|/p_{\max}$) for the water-only and transcranial cases are shown in Figs. 6(a1) and 6(a2), respectively. We can identify that the designed hologram generates a void-containing beam whose pressure peaks around the focal distance ($z = 96.9$ mm for the water-only case and $z = 98.3$ mm for the transcranial case). The transverse field profiles, measured at $z = F$, are given in
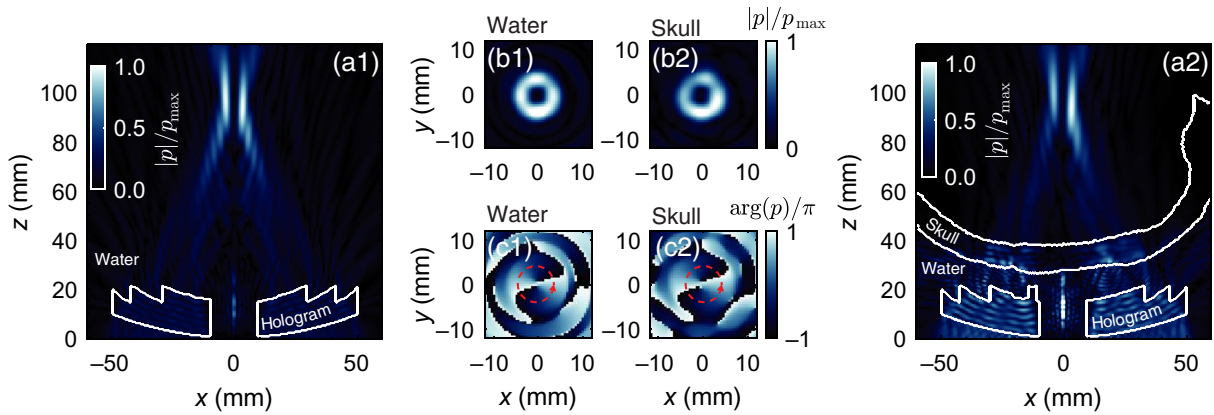
FIG. 6.  Simulated fields of vortex holograms ($l = 2$) designed for water-only and transcranial-propagation media. (a1) Water-only and (a2) transcranial normalized sagittal cross sections of the field at $y = 0$. (b1,c1) Water-only and (b2,c2) transcranial magnitude and phase, respectively, of a transverse cross section of the field obtained at $z = F$.

Figs. 6(b1), 6(b2), 6(c1), and 6(c2). The magnitudes of the water-only and transcranial fields [Figs. 6(b1) and 6(b2)] show a ring-shaped distribution, and at its center the field vanishes. The null is caused by the phase singularity at the focal spot, which is clearly visible in Figs. 6(c1) and 6(c2) for the water-only and transcranial cases, respectively. In addition, we can identify that the phase singularity is the result of a screw dislocation produced by the counterclockwise rotation of the phase, marked by the red arrows.

In Fig. 7(a), the magnitude of the field is shown in detail for a transverse section. The water-only and transcranial fields agree, and the beam shows a width of 7.4 mm (2.5 times the wavelength at the nominal frequency). The phase as a function of the azimuthal angle at a radial distance of 3.7 mm, corresponding to half the beam width, is shown in detail in Fig. 7(b). The generated transverse field shows a levorotatory phase distribution whose phase rotates as a function of the azimuthal angle at a rate given by the topological charge, $l = 2$. Therefore, the phase rotates by $4\pi$ times in a complete azimuthal turn, and the water-only and transcranial results agree to high accuracy. Finally, the longitudinal cross section of the field along the axial coordinate, measured at $y = -3.7$ mm and $x = 0$ mm (matching the peak pressure location), is shown in Fig. 7(c), where both the water-only and the transcranial holograms show very similar focusing.
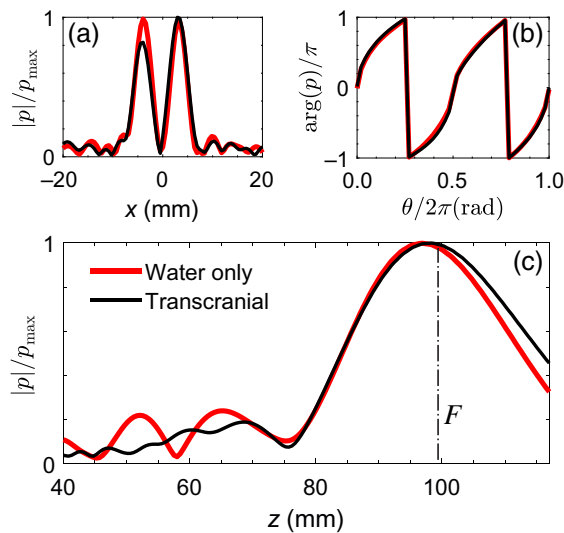


FIG. 7.  Detailed cross-section view of the pressure fields for the water-only (red continuous line) and transcranial (black continuous line) holograms for the higher topological charge $l = 2$. (a) Normalized magnitude of the field at $z = F$ and $y = 0$. (b) Normalized phase of the field versus the azimuthal angle. (c) Axial cross section of the field simulated at $y = -3.7$ and $x = 0$ mm.

[1] W. J. Elias, D. Huss, T. Voss, J. Loomba, M. Khaled, E. Zadicario, R. C. Frysinger, S. A. Sperling, S. Wylie, S. J. Monteith, *et al.*, A pilot study of focused ultrasound thalamotomy for essential tremor, N. Engl. J. Med. **369**, 640 (2013).

[2] Y. Tufail, A. Yoshihiro, S. Pati, M. M. Li, and W. J. Tyler, Ultrasonic neuromodulation by brain stimulation with transcranial ultrasound, Nat. Protoc. **6**, 1453 (2011).

[3] N. Lipsman, Y. Meng, A. J. Bethune, Y. Huang, B. Lam, M. Masellis, N. Herrmann, C. Heyn, I. Aubert, A. Boutet, *et al.*, Blood–brain barrier opening in Alzheimer's disease using MR-guided focused ultrasound, Nat. Commun. **9**, 1 (2018).

[4] Y. Su, J. Ma, L. Du, J. Xia, Y. Wu, X. Jia, Y. Cai, Y. Li, J. Zhao, and Q. Liu, Application of acoustic radiation force impulse imaging (ARFI) in quantitative evaluation of neonatal brain development, Clin. Exp. Obstet. Gynecol. **42**, 797 (2015).

[5] J. F. Nye and M. V. Berry, in *Mathematical, Physical Sciences and Engineering. Roy. Soc. London, London A* (The Royal Society, 1974), Vol. 336, p. 165.

[6] J.-L. Thomas and R. Marchiano, Pseudo Angular Momentum and Topological Charge Conservation for Nonlinear Acoustical Vortices, Phys. Rev. Lett. **91**, 244302 (2003).

[7] K. Volke-Sepúlveda, A. O. Santillán, and R. R. Boullosa, Transfer of Angular Momentum to Matter from Acoustical Vortices in Free Space, Phys. Rev. Lett. **100**, 024302 (2008).

[8] K. Skeldon, C. Wilson, M. Edgar, and M. Padgett, An acoustic spanner and its associated rotational Doppler shift, New J. Phys. **10**, 013018 (2008).

[9] L. Zhang and P. L. Marston, Angular momentum flux of nonparaxial acoustic vortex beams and torques on axisymmetric objects, Phys. Rev. E **84**, 065601 (2011).

[10] A. Anhäuser, R. Wunenburger, and E. Brasselet, Acoustic Rotational Manipulation Using Orbital Angular Momentum Transfer, Phys. Rev. Lett. **109**, 034301 (2012).

[11] C. E. Demore, Z. Yang, A. Volovick, S. Cochran, M. P. MacDonald, and G. C. Spalding, Mechanical Evidence of the Orbital Angular Momentum to Energy Ratio of Vortex Beams, Phys. Rev. Lett. **108**, 194301 (2012).

[12] Z. Hong, J. Zhang, and B. W. Drinkwater, Observation of Orbital Angular Momentum Transfer from Bessel-Shaped Acoustic Vortices to Diphasic Liquid-Microparticle Mixtures, Phys. Rev. Lett. **114**, 214301 (2015).

[13] A. Riaud, M. Baudoin, J.-L. Thomas, and O. B. Matar, Cyclones and attractive streaming generated by acoustical vortices, Phys. Rev. E **90**, 013008 (2014).

[14] J. Wu, Acoustical tweezers, J. Acoust. Soc. Am. **89**, 2140 (1991).

[15] D. Baresch, J.-L. Thomas, and R. Marchiano, Observation of a Single-Beam Gradient Force Acoustical Trap for Elastic Particles: Acoustical Tweezers, Phys. Rev. Lett. **116**, 024301 (2016).

[16] A. Marzo, M. Caleap, and B. W. Drinkwater, Acoustic Virtual Vortices with Tunable Orbital Angular Momentum for Trapping of mie Particles, Phys. Rev. Lett. **120**, 044301 (2018).

[17] Z. Gong and M. Baudoin, Particle Assembly with Synchronized Acoustic Tweezers, Phys. Rev. Appl. **12**, 024045 (2019).

[18] A. Ashkin, Acceleration and Trapping of Particles by Radiation Pressure, Phys. Rev. Lett. **24**, 156 (1970).

[19] D. G. Grier, A revolution in optical manipulation, Nature **424**, 810 (2003).

[20] M. Baudoin, J.-L. Thomas, R. Al Sahely, J.-C. Gerbedoen, Z. Gong, A. Sivery, O. B. Matar, N. Smagin, P. Favreau, and A. Vlandas, Spatially selective manipulation of cells with single-beam acoustical tweezers, Nat. Commun. **11**, 1 (2020).

[21] M. A. Ghanem, A. D. Maxwell, Y.-N. Wang, B. W. Cunitz, V. A. Khokhlova, O. A. Sapozhnikov, and M. R. Bailey, Noninvasive acoustic manipulation of objects in a living body, Proc. Natl. Acad. Sci. USA **117**, 16848 (2020).

[22] D. Baresch and V. Garbin, Acoustic trapping of microbubbles in complex environments and controlled payload release, Proc. Natl. Acad. Sci. USA **117**, 15490 (2020).

[23] B. T. Hefner and P. L. Marston, An acoustical helicoidal wave transducer with applications for the alignment of ultrasonic and underwater systems, J. Acoust. Soc. Am. **106**, 3313 (1999).

[24] R. Marchiano and J.-L. Thomas, Synthesis and analysis of linear and nonlinear acoustical vortices, Phys. Rev. E **71**, 066616 (2005).

[25] J. F. Pazos-Ospina, J. L. Ealo, and E. E. Franco, Characterization of phased array-steered acoustic vortex beams, J. Acoust. Soc. Am. **142**, 61 (2017).

[26] J. L. Ealo, J. C. Prieto, and F. Seco, Airborne ultrasonic vortex generation using flexible ferroelectrets, IEEE Trans. Ultrason. Ferroelectr. Freq. Control **58**, 1651 (2011).

[27] N. Jiménez, R. Picó, V. Sánchez-Morcillo, V. Romero-García, L. M. García-Raffi, and K. Staliunas, Formation of high-order acoustic Bessel beams by spiral diffraction gratings, Phys. Rev. E **94**, 053004 (2016).

[28] T. Wang, M. Ke, W. Li, Q. Yang, C. Qiu, and Z. Liu, Particle manipulation with acoustic vortex beam induced by a brass plate with spiral shape structure, Appl. Phys. Lett. **109**, 123506 (2016).

[29] N. Jiménez, V. Romero-García, L. M. García-Raffi, F. Camarena, and K. Staliunas, Sharp acoustic vortex focusing by Fresnel-spiral zone plates, Appl. Phys. Lett. **112**, 204101 (2018).

[30] S. Gspan, A. Meyer, S. Bernet, and M. Ritsch-Marte, Optoacoustic generation of a helicoidal ultrasonic beam, J. Acoust. Soc. Am. **115**, 1142 (2004).

[31] R. D. Muelas-Hurtado, J. L. Ealo, J. F. Pazos-Ospina, and K. Volke-Sepúlveda, Generation of multiple vortex beam by means of active diffraction gratings, Appl. Phys. Lett. **112**, 084101 (2018).

[32] X. Jiang, Y. Li, B. Liang, J.-C. Cheng, and L. Zhang, Convert Acoustic Resonances to Orbital Angular Momentum, Phys. Rev. Lett. **117**, 034301 (2016).

[33] L. Ye, C. Qiu, J. Lu, K. Tang, H. Jia, M. Ke, S. Peng, and Z. Liu, Making sound vortices by metasurfaces, AIP Adv. **6**, 085007 (2016).

[34] A. Marzo, A. Ghobrial, L. Cox, M. Caleap, A. Croxford, and B. Drinkwater, Realization of compact tractor beams using acoustic delay-lines, Appl. Phys. Lett. **110**, 014102 (2017).

[35] C. J. Naify, C. A. Rohde, T. P. Martin, M. Nicholas, M. D. Guild, and G. J. Orris, Generation of topologically diverse acoustic vortex beams using a compact metamaterial aperture, Appl. Phys. Lett. **108**, 223503 (2016).

[36] H. Esfahlani, H. Lissek, and J. R. Mosig, Generation of acoustic helical wavefronts using metasurfaces, Phys. Rev. B **95**, 024312 (2017).

[37] K. Melde, A. G. Mark, T. Qiu, and P. Fischer, Holograms for acoustics, Nature **537**, 518 (2016).

[38] S. Jiménez-Gambín, N. Jiménez, J. M. Benlloch, and F. Camarena, Generating Bessel beams with broad depth-of-field by using phase-only acoustic holograms, Sci. Rep. **9**, 1 (2019).

[39] C. Horodyckid, M. Canney, A. Vignot, R. Boisgard, A. Drier, G. Huberfeld, C. François, A. Prigent, M. D. Santin, C. Adam, *et al.*, Safe long-term repeated disruption of the blood-brain barrier using an implantable ultrasound device: A multiparametric study in a primate model, J. Neurosurg. **126**, 1351 (2017).

[40] A. Idbaih, M. Canney, L. Belin, C. Desseaux, A. Vignot, G. Bouchoux, N. Asquier, B. Law-Ye, D. Leclercq, A. Bissery, *et al.*, Safety and feasibility of repeated and

transient blood–brain barrier disruption by pulsed ultrasound in patients with recurrent glioblastoma, Clin. Cancer Res. **25**, 3793 (2019).

[41] A. Abrahao, Y. Meng, M. Llinas, Y. Huang, C. Hamani, T. Mainprize, I. Aubert, C. Heyn, S. E. Black, K. Hynynen, *et al.*, First-in-human trial of blood–brain barrier opening in amyotrophic lateral sclerosis using MR-guided focused ultrasound, Nat. Commun. **10**, 1 (2019).

[42] C. Shen, J. Xu, N. X. Fang, and Y. Jing, Anisotropic Complementary Acoustic Metamaterial for Canceling out Aberrating Layers, Phys. Rev. X **4**, 041033 (2014).

[43] G. Maimbourg, A. Houdouin, T. Deffieux, M. Tanter, and J.-F. Aubry, 3D-printed adaptive acoustic lens as a disruptive technology for transcranial ultrasound therapy using single-element transducers, Phys. Med. Biol. **63**, 025026 (2018).

[44] S. Jiménez-Gambín, N. Jiménez, J. M. Benlloch, and F. Camarena, Holograms to Focus Arbitrary Ultrasonic Fields through the Skull, Phys. Rev. Appl. **12**, 014016 (2019).

[45] U. Schneider, E. Pedroni, and A. Lomax, The calibration of CT hounsfield units for radiotherapy treatment planning, Phys. Med. Biol. **41**, 111 (1996).

[46] T. D. Mast, Empirical relationships between acoustic parameters in human soft tissues, Acoust. Res. Lett. Online **1**, 37 (2000).

[47] M. Tabei, T. D. Mast, and R. C. Waag, A k-space method for coupled first-order acoustic propagation equations, J. Acoust. Soc. Am. **111**, 53 (2002).

[48] B. E. Treeby and B. Cox, Modeling power law absorption and dispersion for acoustic propagation using the fractional laplacian, J. Acoust. Soc. Am. **127**, 2741 (2010).

[49] B. E. Treeby, J. Jaros, A. P. Rendell, and B. Cox, Modeling nonlinear ultrasound propagation in heterogeneous media with power law absorption using ak-space pseudospectral method, J. Acoust. Soc. Am. **131**, 4324 (2012).

[50] G. Maimbourg, A. Houdouin, T. Deffieux, M. Tanter, and J.-F. Aubry, Steering capabilities of an acoustic lens for transcranial therapy: Numerical and experimental studies, IEEE Trans. Biomed. Eng. **67**, 27 (2019).

[51] N. Jiménez, F. Camarena, J. Redondo, V. Sánchez-Morcillo, Y. Hou, and E. E. Konofagou, Time-domain simulation of ultrasound propagation in a tissue-like medium based on the resolution of the nonlinear acoustic constitutive relations, Acta Acust. United Ac. **102**, 876 (2016).

[52] M. Ferri, J. M. Bravo, J. Redondo, S. Jiménez-Gambín, N. Jiménez, F. Camarena, and J. V. Sánchez-Pérez, On the evaluation of the suitability of the materials used to 3D print holographic acoustic lenses to correct transcranial focused ultrasound aberrations, Polymers **11**, 1521 (2019).

[53] J. Hill, Physical activity and obesity, Lancet **363**, 182 (2004).

[54] A. Bouakaz and J.-M. Escoffre, *Therapeutic Ultrasound* (Springer, Cham, Switzerland, 2016).

[55] R. S. Cobbold, *Foundations of Biomedical Ultrasound* (Oxford University Press, New York, 2006).